International Journal of Applied Earth Observations and Geoinformation 101 (2021) 102347

Contents lists available at ScienceDirect

International Journal of Applied Earth Observations and Geoinformation

journal homepage: www.elsevier.com/locate/jag

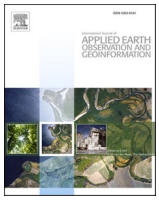

Sentinel-2 MSI data for active fire detection in major fire-prone biomes: A multi-criteria approach

Xikun Hu, Yifang Ban *, Andrea Nascetti

Division of Geoinformatics, KTH Royal Institute of Technology, Stockholm 10044, Sweden

ARTICLE INFO

Keywords:
Sentinel-2
MultiSpectral instrument
Active fire detection
Biome
Multi-criteria

ABSTRACT

Sentinel-2 MultiSpectral Instrument (MSI) data exhibits the great potential of enhanced spatial and temporal coverage for monitoring biomass burning which could complement other coarse active fire detection products. This paper aims to investigate the use of reflective wavelength Sentinel-2 data to classify unambiguous active fire areas from inactive areas at 20 m spatial resolution. A multi-criteria approach based on the reflectance of several bands (i.e. B4, B11, and B12) is proposed to demonstrate the boundary constraints in several representative biomes. It is a fully automatic algorithm based on adaptive thresholds that are statistically determined from 11 million Sentinel-2 observations acquired over corresponding summertime (June 2019 to September 2019) across 14 regions or countries. Biome-based parameterizations avoid high omission errors (OE) caused by small and cool fires in different landscapes. It also takes advantage of the multiple criteria whose intersection could reduce the potential commission errors (CE) due to soil dominated pixels or highly reflective building rooftops. Active fire detection performance was mainly evaluated through visual inspection on eight illustrative subsets because of unavailable ground truth. The detection results revealed that CE and OE could be kept at a low level with 0.14 and 0.04 as an acceptable trade-off. The proposed algorithm can be employed for rapid active fire detection as soon as the image is obtained without the requirement of using multi-temporal imagery, and can even be adapted to onboard processing in the future.

1. Introduction

Biomass burning in fire-prone regions around the world has generated large research interest for many years (Matson and Holben, 1987; Setzer and Pereira, 1991; Scholes et al., 1996; Bowman et al., 2017). Earth Observation satellites have been employed to systematically monitor fire activity over large regions in two ways: (i) to map the spatial extent of the burned scars (during or after the event), and (ii) to detect the location of actively burning spots (during the fire event). Specifically, active fire detection lies at the focus of current research on early warning fire alert and dedicated wildfire monitoring.

Existing global active fire monitoring products mainly use data from low spatial resolution polar-orbiting satellite (e.g. 1 km) or geostationary satellites (e.g. 2 km) with middle-infrared (3–4 μm) and thermal-infrared (10–12 μm) bands (Stroppiana et al., 2000), which are optimal for thermal anomaly detection. Therefore, present active fire detection algorithms are typically developed based on these sensors such as Advanced Very High Resolution Radiometer (AVHRR), Moderate Resolution Imaging Spectroradiometer (MODIS), Visible Infrared Imaging Radiometer Suite (VIIRS), Sentinel-3 Sea and Land Surface Temperature Radiometer (SLSTR) (Stroppiana et al., 2000; Wooster et al., 2012; Schroeder et al., 2014; Giglio et al., 2016). Giglio et al. (2016) released an active fire product as part of the MODIS Collection 6 land-product reprocessing, which addressed some limitations of commission errors (CE) and omission errors (OE) in the previous active fire product. Similar to MODIS, a VIIRS 375 m active fire detection algorithm takes advantages of the gain thermal infrared (11.45 μm) and mid-infrared (3.74 μm) channel data, thus providing a large range of fire pixel radiances (Schroeder et al., 2014). SLSTR instrument includes low-gain middle infrared and thermal IR channels (1 km) that can avoid detector saturation over even high-intensity fires as well as short wave infrared (SWIR) channels (500 m) at night to compensate for thermal hotspots discrimination (Wooster et al., 2012). In addition, Visible and Infra-Red Radiometer (VIRR) onboard the FengYun-3C satellite showed the feasibility of active fire detection with 1 km resolution via identifying the slope of brightness temperatures in mid-infrared (3.55–3.93 μm) and thermal infrared (10.3–11.3 μm) bands (Lin et al., 2018). To complement existing satellite fire product, geostationary sensors were also

* Corresponding author.
E-mail address: yifang@kth.se (Y. Ban).

https://doi.org/10.1016/j.jag.2021.102347
Received 10 August 2020; Received in revised form 17 January 2021; Accepted 18 April 2021
Available online 21 May 2021

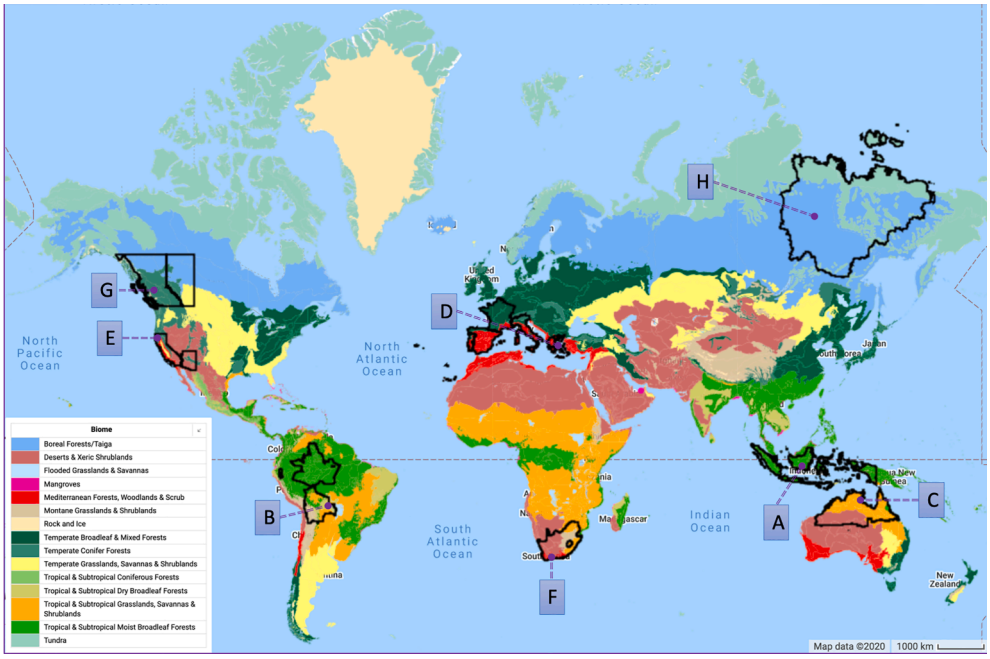

Fig. 1. The 14 ROIs (with black polygon) where Sentinel-2 MSI TOA observation samples between June and September were extracted. 8 illustrative subsets are pointed by purple dots (from A to H). Base map is the RESOLVE Ecoregions from GEE, adapted from (Dinerstein et al., 2017).

exploited in active fire detection with high temporal resolution (Roberts and Wooster, 2014; Hall et al., 2019) like GOES-16 Advanced Baseline Imager (ABI) and Spinning Enhanced Visible and Infra-Red Imager (SEVIRI).

Although the coarse resolution polar-orbiting and geostationary sensors mentioned above have consistent global monitoring in near-real-time (NRT) for rapid response, their large instantaneous field of view (IFOV) impedes hot target detection. In other words, background radiance tends to exceed the signal from the subtle hot targets using a large IFOV, which makes it difficult to retrieve targets' sub-pixel spatial information in size from satellite image (Murphy et al., 2016). Therefore, there remains a need for complementary approaches to detect active fires with more detailed context information for decision-making and interpretation (Davies et al., 2009).

With higher spatial resolution, open-access multi-spectral imagery available from the Landsat series of satellites since 1972 and Sentinel-2 satellites (i.e. 2A and 2B) since 2015 provides an alternative approach that supplements present active fire products with the ability of medium resolution global land surface monitoring (Csiszar and Schroeder, 2008; Schroeder et al., 2016; Murphy et al., 2016; Kumar and Roy, 2018). As the latest satellite in the Landsat series, Operational Land Imager (OLI) sensor in Landsat-8 offers 16-day repetitive Earth coverage and collects image data for 9 spectral bands with a 30-meter spatial resolution for all bands except the 15-meter panchromatic band (USGS, 2019). Compared to the Landsat sensors, each of the two Sentinel-2 satellites carries a wide-swath Multispectral Instrument (MSI), characterized by enhanced revisit times time (5 days or less) and 13 spectral bands from visible (VIS) and near-infrared (NIR), to SWIR at 10, 20, 60 spatial resolutions (Drusch et al., 2012). The combination of Landsat-8, Sentinel-2A, and Sentinel-2B can provide a global revisit interval of 2.9 days in median average (Li and Roy, 2017). Collectively, satellite-based spatially-refined active fire detections could be achieved by integrating all available multi-spectral instruments to facilitate NRT active fire monitoring from coarse to medium resolution (Schroeder et al., 2016). Sentinel-2 MSI, even if lacks 4 μm and 10–12 μm bands which are included in other coarse-resolution sensors, have two SWIR bands that can potentially offer significantly improved mapping capability that generates detailed fire line information (Schroeder et al., 2016). These two channels around 1.6 and 2.2 μm can be used for hot target detection, as these spectral regions suffer little attenuation of reflectance through the atmosphere (Murphy et al., 2016). The summary of spectral bands used in active fire detection products can be found in Table A.5.

To investigate the complementary roles of multi-spectral satellite data on active fire detection, Landsat-8 OLI was typically employed to locate active fire spots more accurately at 30 m spatial resolution (Schroeder et al., 2016; Murphy et al., 2016; Kumar and Roy, 2018). Several active fire detection algorithms were developed using reflective wavelength bands (Csiszar and Schroeder, 2008; Giglio et al., 2008; Schroeder et al., 2016; Murphy et al., 2016; Kumar and Roy, 2018). Among them, the latest GOLI algorithm proposed by Kumar and Roy (2018) showed comparable CE but slightly lower OE than other algorithms proposed in Schroeder et al. (2016) and Murphy et al. (2016). Based on 39 million reflectance observation samples from three winter and three summer months across the United States, GOLI determined fixed criteria thresholds derived through a statistical examination on top of atmosphere (TOA) Landsat-8 reflectance of Red band (B4: 0.66 μm) and SWIR2 (B7: 2.20 μm) using ordinary least squares (OLS) regression that was rarely used by other Landsat-8 active fire detection algorithms such as Schroeder et al. (2016) and Murphy et al. (2016). However, due to the system limitation of the Landsat-8 sensor, it is still a problem that under some extreme conditions (e.g. large fires or volcanic events) when a detector views an object that is much brighter than the maximum radiance that the instrument was designed to handle, the detector's pixel values can roll over the 12-bit limit to a very small integer (not necessarily just a value of 0) (USGS, 2019). Schroeder et al. (2016) observed that the core area of active fire would show near-zero and artificially low B7 radiance values surrounded by other pixels at or above the maximum saturation of 24.3 W/(m^2 sr μm), therefore describing a typical over-saturation scenario for Landsat-8 OLI data. The over-saturated longer wavelength of B7 of GOLI algorithm might hinder sufficient active fire discrimination when the fire was obscured by optically thick smoke (i.e. OE), even though the shorter SWIR1 (B6: 1.61 μm) has been employed as the complement to catch the pixels folded.

In recent years, the majority of wildfire studies using Sentinel-2 have been concentrated on burned area mapping algorithms and products (Fernández-Manso et al., 2016; Huang et al., 2016; Navarro et al., 2017;

Table 1
Overview of the biome with the corresponding number of samples and specific illustrative subsets. The observation samples extracted randomly from the whole 15,642 tiles of Sentinel-2 during the summer months from 14 ROIs.

Biome	No. Samples	Illustrative subsets
Tropical & Subtropical Moist Broadleaf Forests	2,338,032	A
Tropical & Subtropical Dry Broadleaf Forests	391,997	B
Tropical & Subtropical Grasslands, Savannas & Shrublands	916,362	C
Mediterranean Forests, Woodlands & Scrub	3,117,755	D E F
Temperate Conifer Forests	1,186,385	G
Boreal Forests/Taiga	847,608	H
Deserts & Xeric Shrublands	1,355,334	
Temperate Broadleaf & Mixed Forests	427,826	
Temperate Grasslands, Savannas & Shrublands	385,874	
Tundra	230,836	
Montane Grasslands & Shrublands	180,931	
Flooded Grasslands & Savannas	52,712	
Mangroves	2,434	
Tropical & Subtropical Coniferous Forests	2,216	

Quintano et al., 2018; Roteta et al., 2019). Compared to Landsat-8, Sentinel-2A and Sentinel-2B together provide higher temporal resolution and higher spatial resolution. In addition, B12 of Sentinel-2 MSI represents the maximum saturation level of 24.5 W/(m^2 sr μm), a relatively similar radiance sensibility with B7 of Landsat-8 OLI (Zhang et al., 2018). Differently, a saturation pixel value of B12 could be assigned to the flaming fire hotspots if radiance is greater than that maximum. Until now, very few studies were conducted on active fire detection using Sentinel-2 data.

Therefore, this study investigates the complementary role of 20 m resolution Sentinel-2 multispectral data for active fire detection, focusing on the development of an effective detection algorithm. The research has promising potential for enhancing spatial and temporal coverage in medium resolution across large scales even globally in NRT through the fusion of Sentinel-2 and Landsat-8, even future Landsat-9 satellites.

2. Study areas and data characteristics

2.1. Study areas

Fourteen regions of interest (ROIs) representing different biomes were selected to characterize a wide range of vegetation conditions and fire-prone areas that suffered from forest fires frequently or seasonally, as shown in Fig. 1 and Table 1. The ROIs include Southern Kalimantan, Indonesia, California and Arizona states in the US, British Columbia (BC) and Alberta in Canada, Northern Australia, South Africa, Amazonas state in Brazil, Bolivia, and several European countries (Portugal,

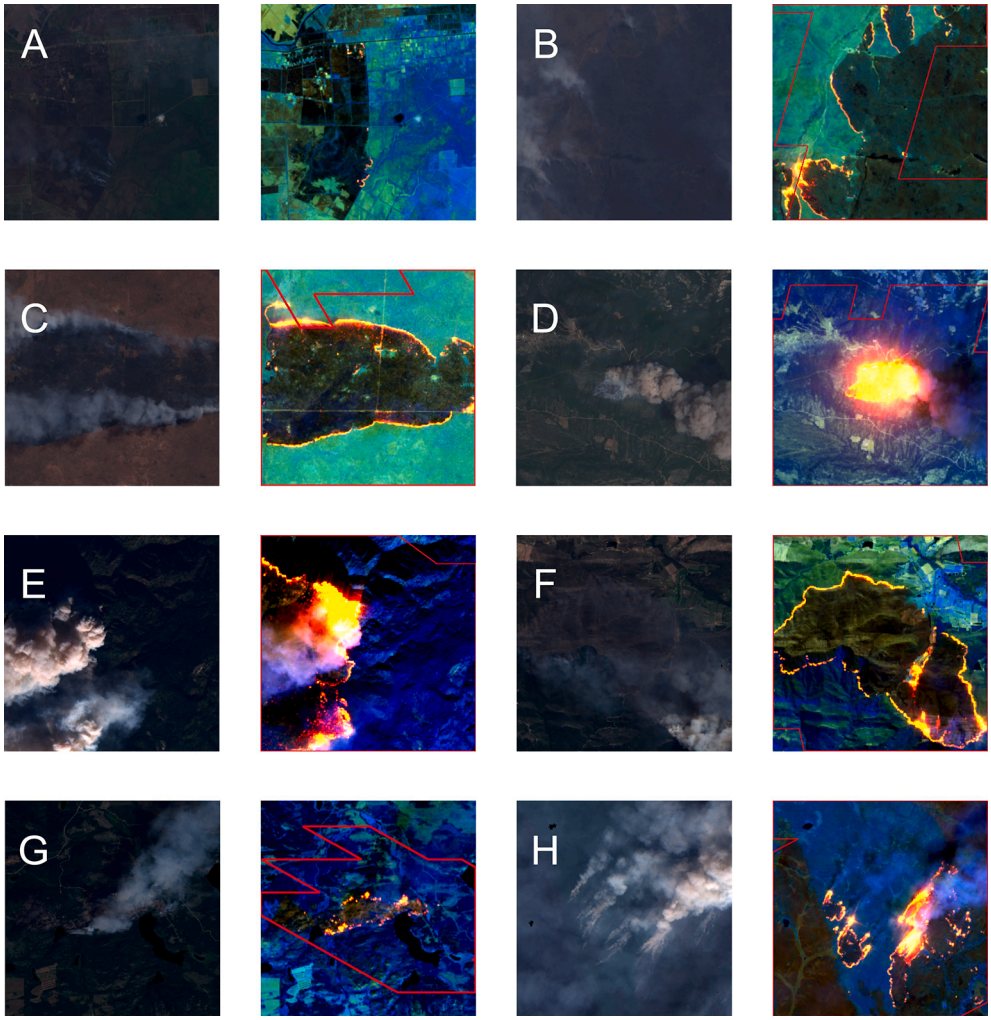

Fig. 2. Illustrative Sentinel-2 reflectance for subsets in Fig. 1. For A-H, each figure in left had 0.66, 0.56, and 0.49 μm shown as RGB, respectively and right one had 2.20, 1.61, and 0.86 μm displayed in RGB, respectively). Red lines drew the coarse perimeters from the FIRMS in spatial resolution of 1,000 meters. Figures appear in color the online version.

Table 2
Sentinel-2 Image location and acquisition date of the 8 illustrative fire events.

	S2 IMG. LOC.	Acquisition Date/ (Year-Month-Day)	Country
A	South Kalimantan	2018-09-28	Indonesia
B	Charagua	2019-08-21	Bolivia
C	Roper Gulf	2018-08-29	Australia
D	Geraneia	2018-07-23	Greece
E	Camp Fire	2018-11-11	United States
F	George	2018-10-25	South Africa
G	Bulkley-Nechako	2018-08-08	Canada
H	Verkhnevilyuysky	2018-07-19	Russia

France, Italy, Greece, Spain). In recent year, the world witnessed numerous wildfires that resulted in huge human, economic and environmental losses. For example, BC and Alberta saw thousands of fires every year after a very dry winter and spring, followed by record lightning strikes (Government of Canada, 2020). The 2019 Amazon rain forest saw huge fires in Amazonas state and Bolivia that ravaged more than several million hectares of land (Yeung, 2019). Further, an unprecedented amount of wildfires had been raging in various regions of the Arctic, including Siberia, Sweden, Greenland, and Alaska in the US (ESA, 2019). Therefore, we included new fire-prone regions in Siberia in this study in addition to these typical regions analyzed in previous studies (Schroeder et al., 2016; Kumar and Roy, 2018). Wildfires are rare in Siberia but the year 2019 saw hundreds of wildfires burning millions of hectares, which raised public attention to care about climate change in the Arctic Circles (Wikipedia, 2019)

Eight illustrative fire events (A to H) were selected to validate the performance of our proposed active fire detection algorithm (Fig. 1). They include South Kalimantan, Indonesia (A, centered on Lon: 114.777, Lat: −3.251), Charagua, Bolivia (B, −60.616, −15.624), Roper Gulf, Australia (C, 136.089, −15.676), Geraneia (D, 23.166, 38.010), the Camp Fire, United States (E, −121.390, 39.813), George, South Africa (F, 22.431, −33.870), Bulkley-Nechako, Canada (G, −125.947, 53.846), and Verkhnevilyuysky, Russia (H, 119.99, 65.47). In corresponding Fig. 2, the true-color and false-color images of illustrative subsets are shown with the area of 6,000 × 6,000 meters. For each false-color image, the MODIS MCD14DL NRT active fire detection at 1 km resolution (Giglio et al., 2003; Justice et al., 2011) shown as red polygons were provided by the Fire Information for Resource Management System (FIRMS). In general, fire ecologists and researchers working on active fire detection algorithms classify fires into flaming (1,000 K) and smoldering fires (600 K) (Giglio et al., 2008), depending on their temperatures. In our study, subset A might contain hot soil that would be misclassified as hotspots. Subsets C and G consist of possible smoldering fires except for the obvious flames. On the other hand, large flames in subsets D, E, and H would result in the most false fire pixels that occur along the ambiguous fire boundaries.

2.2. Data characteristics

In this study, 15,642 tiles of Sentinel-2 MSI images during the summer months from 14 ROIs were downloaded from Google Earth Engine (GEE) for the active fire algorithm development. Over 11 millions of observation samples were extracted randomly from the whole 15,642 tiles (Table 1). Table 2 provides a summary of the Sentinel-2 image location and acquisition date for the 8 illustrative fire events.

Giglio et al. (2008) pioneered the use of TOA reflectance for the detection of hot targets in 30-m spatial resolution daytime imagery with ASTER sensor. Murphy et al. (2016), Schroeder et al. (2016), and Kumar and Roy (2018) used Landsat-8 OLI TOA reflectance as input for active fire detection. Furthermore, sensor-to-sensor inter-calibration results show a good agreement of the TOA reflectance between Sentinel-2A MSI and Landsat-8 OLI over the VIS and NIR (VNIR) and SWIR spectral ranges (Gascon et al., 2017; Van Der Werff and Van Der Meer, 2016). To keep the consistency of algorithm development and facilitate further

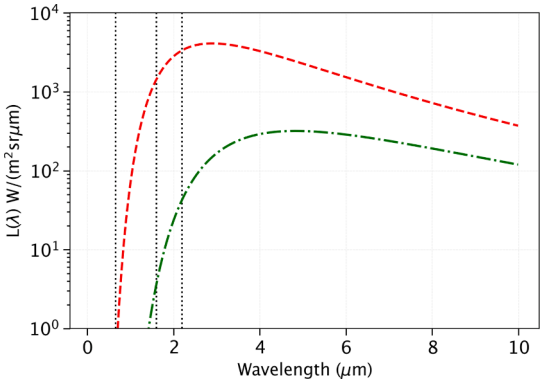

Fig. 3. Spectral radiance for 1000 K flaming (dashed red curve) and 600 K smoldering fires (dash-dotted green curve) in the wavelength domain based on Planck function. In this idealized case, we assumed the land surface to be a black body with no atmospheric extinction. Vertical dotted lines indicate wavelength locations of Sentinel-2 B4, 11, and B12, respectively.

comparison, Sentinel-2 Level-1C (L1C) TOA spectral reflectance data are used in this study. The physical values range from 1 (minimum reflectance 10^{-4}) to 10,000 (reflectance 1), but values higher than 1 can be observed in some cases due to specific angular reflectivity effects (Gascon et al., 2017). These reflectance values will include contributions from clouds and atmospheric aerosols and gases. In this study, only cloud-free observations reflectance samples were extracted, where the Bit 10 and 11 of QA60 band were labeled as 0 (no opaque and cirrus clouds) together.

Table 1 listed the number of TOA observation samples from all ROIs for each biome. Major biomes have their specific ecological and distribution characteristics to the fire regime (Bond et al., 2005). The tropical grasslands and savannas, Mediterranean shrublands, and boreal forests belong to the world's major biomes that experience frequent and/or predictable fire. The temperate conifer forest is additionally investigated in particular.

Table 1 also introduced the representative biome for each illustrative subset. For instance, in tropical & subtropical regions, the biome types of A, B, and C are moist broadleaf forests, dry broadleaf forests, and grasslands, savannas & shrublands, respectively. D, E, and F have the same biome, namely Mediterranean Forests, Woodlands & Scrub, even though they are situated in different hemispheres. The other biome types are not considered as illustrative tests in this study since most of them are not prone to fire. It should be noted that the definition of Sentinel-2 subsets in Fig. 2 was different from ROIs in Fig. 1; Sentinel-2 subsets in Fig. 2 were test images used to validate the performance of the proposed algorithm, while the ROIs in Fig. 1 were regions/countries where the 11 million observation samples were collected to determine the algorithm parameterizations criteria of the corresponding biome.

3. Methods

The proposed active fire detection (AFD-S2) algorithm is a multi-criteria approach based on the statistical regression of the reflectance of several Sentinel-2 bands (i.e. B4, B11, and B12). The main advantages of the AFD-S2 detection algorithm are: (i) fully automatic algorithm based on adaptive thresholds for each biome class (ii) good accuracy with a balanced amount of omission and commission errors (iii) fast computation without the requirement of using multi-temporal imagery and suitable for future satellite on-board processors.

3.1. AFD-S2 algorithm theoretical background

The emitted energy from active fires increases rapidly at the SWIR wavelength based on Planck function, therefore, the active fire detection

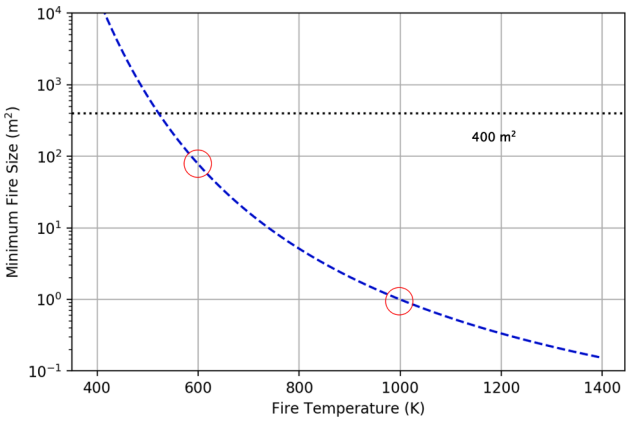

Fig. 4. Minimum fire size required to saturate Sentinel-2 B12 as a function of fire temperature. A surface reflectance of 15% was assumed.

algorithms may identify hot and large anomalies (Giglio and Justice, 2003). Planck's radiation law is the fundamental theory to detect active forest fire (Giglio et al., 2008). It describes the spectral radiance emitted by a black body for wavelength λ at temperature t as the formula shown below:

$$L(\lambda, t) = \frac{c_1}{\lambda^5 (e^{c_2/\lambda t} - 1)} \quad (1)$$

where c_1 and c_2 are constants. $L(\lambda, t)$ denotes black-body radiance in W/(m^2 sr μm). λ is the wavelength in μm. t is the temperature (K). In Fig. 3, the ratio L(λ) is shown for representative flaming (t = 1000 K) and smoldering (t = 600 K) fires at several wavelengths of Sentinel-2 MSI.

The capability of active fire detection is proportional to the amount of emitted energy captured by the satellite sensor. In particular, the amount of energy emitted is related to the fire size and temperature and the measured energy is proportional to the sensor IFOV (Kaufman et al., 1998; Giglio et al., 2008). Higher spatial resolution satellite sensors are more capable of detecting these subtle targets because of their larger proportion of the IFOV occupied by small hot targets. For example, a 20 × 20 m^2 detector of Sentinel-2 sensor has an IFOV that is 2,500 times smaller than that of a 1 × 1 km^2 MODIS detector and a fire with 100 m^2 in size would occupy 25% of the Sentinel-2 IFOV but only 0.01% of MODIS IFOV (Murphy et al., 2016).

In Kumar and Roy (2018), the authors simulated the spectral responses of different fires and observed that fire with a larger size and higher temperature have higher reflectance values in the longer wavelength bands (i.e. SWIR: 2.20 μm and 1.61 μm) and negligible contribution in Red band (0.66 μm). Therefore, a simple approach for active fire detection using Sentinel-2 data is to filter out the pixels with high values in B12 (almost saturated) and low values in B4. A crucial aspect is determining the right threshold to differentiate fire and none fire pixels, accounting for the fire size and temperature required to saturate B12. As will be presented in Section 4.3, active fires tend to saturate B12, especially in the forested regions. Fig. 4 illustrates the simulated minimum fire size required to reach the B12 saturation level of 24.5 W/(m^2 sr μm), revealing that Sentinel-2 can theoretically measure ~1 m^2 flaming fires and smoldering fires about 100 m^2.

However, there are two main issues to be explicitly reported: (i) some soil dominated pixels may have similar spectral responses to the thermal anomalies that will contribute to increasing the amount of CE; (ii) subpixel sized and/or cool thermal anomalies will have a relatively small emitted energy into the SWIR band, compromising the algorithm capability to detect the fire and increasing the OE. To reduce OE, we attempt to focus on the single criteria using lower 3σ prediction interval of OLS regressions of B4 and B12 based on typical biome property rather than mixing different soil and vegetation types together in Kumar and Roy (2018). The low reflectance of B4 and the relatively high reflectance

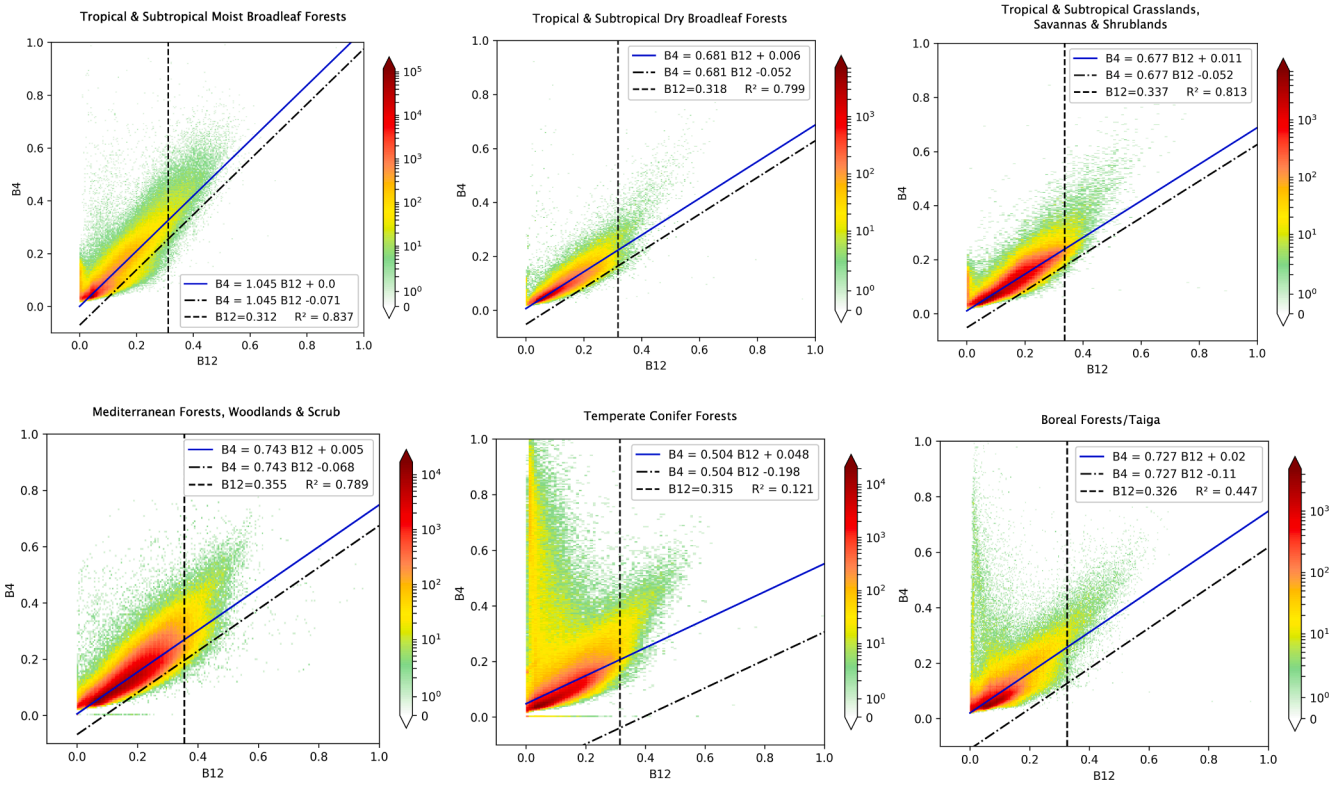

Fig. 5. OLS regressions of the plotted data grouped by biome were shown by the blue lines; the lower 3σ prediction intervals were shown by the dash-dotted lines. The derived thresholds for B12 from Eq. (4) were represented by the dashed vertical lines. The bottom-right space far away dash-dotted line or dashed vertical line means the spectral distribution (B4 vs B12) of possible unambiguous active fire pixels if they exist. The figures appear in color in the online version.

of B12 can effectively help identify cool thermal pixels. On the other hand, the additional joint criteria are involved for the specific biome to reduce the CE, since the intersection among multiple criteria could enhance the active fire pixels' detection. Two subsets are used to test these cases: (i) Subset C had cool smoldering biomass burning inside the burned areas rather than the fire fronts (ii) subset A is characterized by soil areas without thermal anomalies.

3.2. Data preparation

All Sentinel-2 data was downloaded using GEE platform. The observation samples were extracted over the land surface during the summer season systematically. The main procedures consist of the following four steps, (i) successively getting the Sentinel-2 TOA imageries covering ROIs (see Fig. 1) during the summer months in 2019; (ii) sorting out imagery scenes and masking clouds based on the QA60 band for each scene to get the cloud-free imagery; (iii) extracting a stratified random sample of points (No. 100 to 200) from the cloud-free image with a nominal scale of 20 meters using the nearest-neighbor re-sampling method; (iv) successively exporting all the pixel samples for each image and ROI collecting the spectral reflectance values and the metadata information (i.e. Image ID, longitude, latitude, acquisition time as well as the specific biome property).

3.3. The AFD-S2 algorithm: a multi-criteria approach

B4 (Red, 0.66 μm) and B12 (SWIR2, 2.20 μm) are primarily selected to detect unambiguous active fires since B4 shows less sensitivity to fire while B12 is less sensitive to atmospheric contamination and highly influenced by a burning fire. The OLS regressions of B4 and B12 for each biome is presented in Fig. 5 plotted as a blue line, where the frequency of occurrence of pixels with the same reflectance is illustrated by colors shaded with a base-10 log scale from white to light blue, blue, yellow, coral, red, and finally, dark red. The coefficients of determination (R^2) are relatively high (except the temperate conifer forests and boreal forests/taiga due to the potential permanent ice in high latitude or on mountains). The primary criterion of AFD-S2 algorithm is derived from spectral scatter-plots between B4 and B12 reflectance values of Sentinel-2 data based on 3σ lower prediction of OLS regression (Eq. (2)) plotted in dash-dotted lines.

$$\rho_{0.66} \leqslant a\rho_{2.20} + b, \tag{2}$$

where $\rho_{2.20}$ and $\rho_{0.66}$ are Sentinel-2 reflectance in B12 and B4, respectively. a and b are coefficient and intercept of 3σ lower prediction band of OLS regression of TOA data grouped by biome in Fig. 5 (e.g. 1.045 and −0.071 in biome of Tropical & Subtropical MOIST Broadleaf Forests). The AFD-S2 algorithm detects the active fire pixels based on the B4-B12 spectral plane areas delineating the burning objects' possible spectral responses. Pixels are considered as active fire if they fall into the constraint-boundary area namely the bottom right part region far away from the dash-dotted line.

In a few specific types of biomes, more criteria are needed to avoid possible CE. Eq. (3) and Eq. (4) can be used to lower the high CE, especially for Mediterranean Forests, Woodlands & Scrub since the hot ashes area around actively burning hotspots would be misclassified as burning pixels. Searching the high B12 and B11 (1.61 μm) reflectance is a good solution to determine the active fire hotspots.

$$\rho_{1.61} \geqslant c, \tag{3}$$

$$\rho_{2.20} \geqslant d, \tag{4}$$

where c and d denote the 0.99 quantiles for B11 and B12 of the grouped data for each biome type, respectively (e.g. the dashed vertical lines in Fig. 5 for B12). Only pixels whose $\rho_{2.20}$ and $\rho_{1.61}$ are larger than the corresponding thresholds are retained. The thresholds of c and d are determined based on a statistical examination for specific biome instead of the globaly fixed thresholds of 0.15 and 0.5 in the Schroeder et al. (2016) and Murphy et al. (2016), respectively, whose criteria use might be either loose or aggressive (Kumar and Roy, 2018).

Furthermore, an ancillary Eq. (5) can deal with remaining sources of CE where $\rho_{2.20}$ should be larger than $\rho_{1.16}$ if the fires occur but the hot soil would not register this property. The ratio factor between $\rho_{2.20}$ and $\rho_{1.16}$ are 1.4 and 1.6 respectively, in the algorithms proposed by Schroeder et al. (2016) and Murphy et al. (2016). For instance, Eq. (5) can be used to reduce the CE in subset A with Tropical & Subtropical Moist Broadleaf Forests.

$$\rho_{2.20}/\rho_{1.61} \geqslant 1, \tag{5}$$

Sometimes, the Boolean operator *OR* would be included to avoid the missing of unambiguous burning pixels through the Eq. (6) as the supplementary criterion for Eq. (3). It can inversely decrease the OE to some extent.

$$\rho_{2.20} \geqslant 1, \tag{6}$$

Overall, the criteria of AFD-S2 for different biomes can be summaries in Table 3. **C1** is the primary criterion whose coefficients and intercepts are calculated based on Eq. (2) as Fig. 5 showed. In addition, for some specific biomes, additional criteria (**C2** and **C3**) are needed to reduce the CE with Boolean "AND" operation. Given the biomes in different regions, the corresponding criteria combinations are suggested to be applied to detect active fires based on **C1** to **C3**. It should be noted that in **C3**, logical "OR" operation is involved to decrease the OE.

Table 3
Criteria of AFD-S2 for different biome.

Biome	C1	C2	C3
Tropical & Subtropical Moist Broadleaf Forests	$\rho_{0.66} \leqslant 1.045\rho_{2.20} - 0.071$	$\rho_{2.20}/\rho_{1.61} \geqslant 1$	
Tropical & Subtropical Dry Broadleaf Forests	$\rho_{0.66} \leqslant 0.681\rho_{2.20} - 0.052$		
Tropical & Subtropical Grasslands, Savannas & Shrublands	$\rho_{0.66} \leqslant 0.677\rho_{2.20} - 0.052$		
Mediterranean Forests, Woodlands & Scrub	$\rho_{0.66} \leqslant 0.743\rho_{2.20} - 0.068$	$\rho_{2.20} \geqslant 0.355$	$\rho_{1.61} \geqslant 0.475$ OR $\rho_{2.20} \geqslant 1.0$
Temperate Conifer Forests	$\rho_{0.66} \leqslant 0.504\rho_{2.20} - 0.198$		
Boreal Forests/Taiga	$\rho_{0.66} \leqslant 0.727\rho_{2.20} - 0.11$		

Table 4
Confusion matrix example.

		Reference Data		
		Active Fire	Non-active Fire	Total
Classified Data	Active Fire	P_{11}	P_{12}	P_{1+}
	Non-active Fire	P_{21}	P_{22}	P_{2+}
	Total	P_{+1}	P_{+2}	N

3.4. Validation matrix and accuracy assessment approaches

The performance of the AFD-S2 algorithm was evaluated by accuracy assessment based on the confusion matrix (Table 4). Two main accuracy metrics OE and CE were computed, as the Eq. (7) and Eq. (8).

$$\mathrm{OE} = P_{21}/P_{+1} \tag{7}$$

$$\mathrm{CE} = P_{12}/P_{1+} \tag{8}$$

We performed a visual interpretation of the Sentinel-2 imagery to

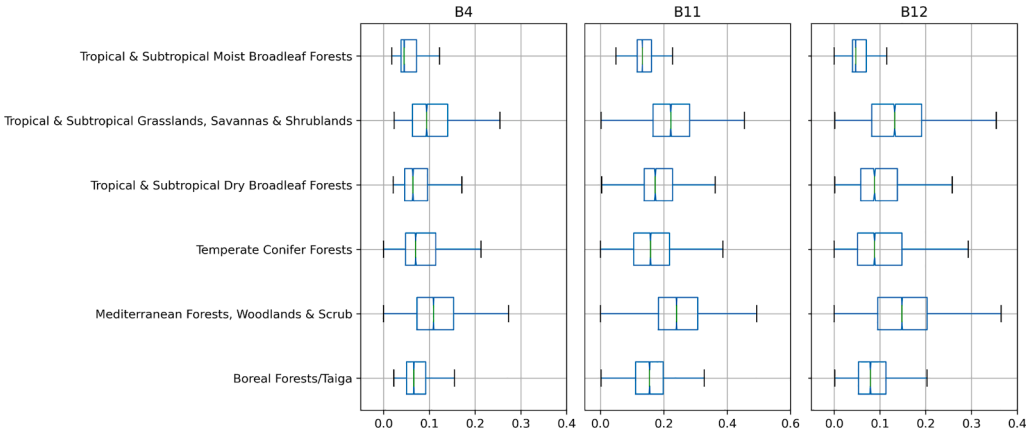

Fig. 6. The boxplot distribution of bands reflectance values within specific biome. The 75th and 25th percentiles are represented by corresponding left and right box edges, respectively. The green line denotes the median value. The outliers outside the minimum and maximum (i.e. two vertical black lines in the endpoints) are ignored.

generate the reference maps of the active fires. The ground truth (GT) masks were preliminarily drawn based on visual inspection of several combinations of Sentinel-2 bands (B12-B11-B12, B12-B11-B8A, and B4-B3-B2). Each pixel of GT was checked carefully through ESA SNAP software to make sure that its spectral values are valid and its distribution is reasonable. Finally, the time-series high-resolution Google Earth base map before and after the fire event were analyzed to refine the GT.

There would be some OE inside hot areas due to the weak penetration in areas covered by dense smoke and CE due to hot ashes area of aerosol around the actively burning hotspots. We attempted to ensure that the GT polygon can include all unambiguous active fire pixels in test images. The accuracy assessment was employed based on the GT and active fire results from the AFD-S2 algorithm according to the validation matrix.

4. Results

4.1. Reflectance statistical analysis in different biomes

The values variation of spectral bands (B4, B11, and B12) in different biomes are presented in Fig. 6 based on the all collected observations for each ROI. The median spectral reflectance values for the three bands are higher (i.e. green line within a boxplot) in the Mediterranean Forests, Woodlands & Scrub regions with respect to other ones. It implies more aggressive criteria (e.g. C2 and C3) are necessary in these regions to reduce possible CE due to the overestimation of active fire points using only the Eq. (2).

In the regions of Tropical & Subtropical Moist Broadleaf Forests, the B4 and B12 reflectance values are characterized by the lowest median (below 0.05) and dispersion. In particular, the active fire detection in this biome would be more affected by soil dominated pixels. Considering that the reflectance value of B11 is relatively higher than the B12, in areas not affected by active fire (i.e. hot soil regions), Eq. (5) reduces the possible commission errors.

4.2. Visual results and comparison of the different criteria

This section presents the visual results obtained in the illustrative subsets reporting the effect of the different proposed criteria for improving active fire detection. Fig. 7 displays the false-color composition, the GT mask, and the corresponding classification outputs for each patch. Accordingly to the biome type and the criteria reported in Table 3, the active fire map can be produced using Eqs. (2)–(6). Qualitatively, the results show that the AFD-S2 algorithm successfully captured the small active fire exploiting the high spatial resolution of Sentinel-2 sensor. It was found that the AFD-S2 results were able to detect the active fire fronts with hgh details, especially for the small fire illustrated in patch A, B, C, F, and G. In Mediterranean-like forest fires in California and Greece (D and E patch) the AFD-S2 multi-criteria approach can filter out the thick blanket of smoke (see true-color map in Fig. 2) and decrease the CE. The first column in Fig. 7 showed the false-color map with RGB composition of B12, B11, and B4, respectively. For each patch, AFD-S2 results detecting the active fire flames and cool smoldering fires are reported in the different columns showing the effect of applying progressively the different criteria. The AFD-S2 final results (i.e. last column for each row) are based on the intersection area of the criteria among **C1**, **C2**, and **C3** as illustrated in Table 3, where each criterion played different roles in the final results to reduce OE and/or CE. For patch A, a map with a green box is the joint intersection of multiple criteria of **C1** and **C2** that additionally reduce the commission errors caused by hot soil pixels. Regarding the patches of B, C, G, and H, the final results are based only on the **C1** approach showing accurate results with low OE (except patch G). For other patches in the Mediterranean Forests, Woodlands & Scrub biome, the final results is the intersection areas based on **C1**, **C2**, and **C3** together, as shown in the maps with a blue box. **C3** leads to more reliable performance through tighter constraint for the flaming fires in Mediterranean forests.

GT based on visual inspection may not reflect 100% real burning condition. However, it still could be regarded as a good alternative reference to assess the algorithm's accuracy. In patch A, the active fire pixels detected were larger than GT but the result of patch B had fewer pixels highlighted as active fire. Regarding the patch D and E, Mediterranean fires always reflect extremely bright flames with high surface reflectance of B11 and B12 around the hot cores which result in large non-active fire areas being detected as active fire pixels, namely high CE. In some cases, it can be accepted as a warning area around the hot cores of a fire outbreak. The fire event F with the Mediterranean biome in South Africa did not produce high CE due to its relatively lower radiation than D and E and disperse actively burning sites with woodlands & scrub. Similarly, G also had divergent burning sites, which caused the possible OE due to the cool smoldering fires after the flames that are excluded by AFD-S2 criteria. In contrast, the obvious CE can be found in H due to the overestimation of the hot ashes area but it is still acceptable accounting for the inner hot areas close to flaming fires.

4.3. Algorithm assessment

The accuracy assessment for each patch can be found in Fig. 8. It can be observed that patches D, E, and F have relatively low OE and CE, which represents that more criteria facilitate the reduction of errors, particularly CE. The highest OE in G is caused by low radiation from

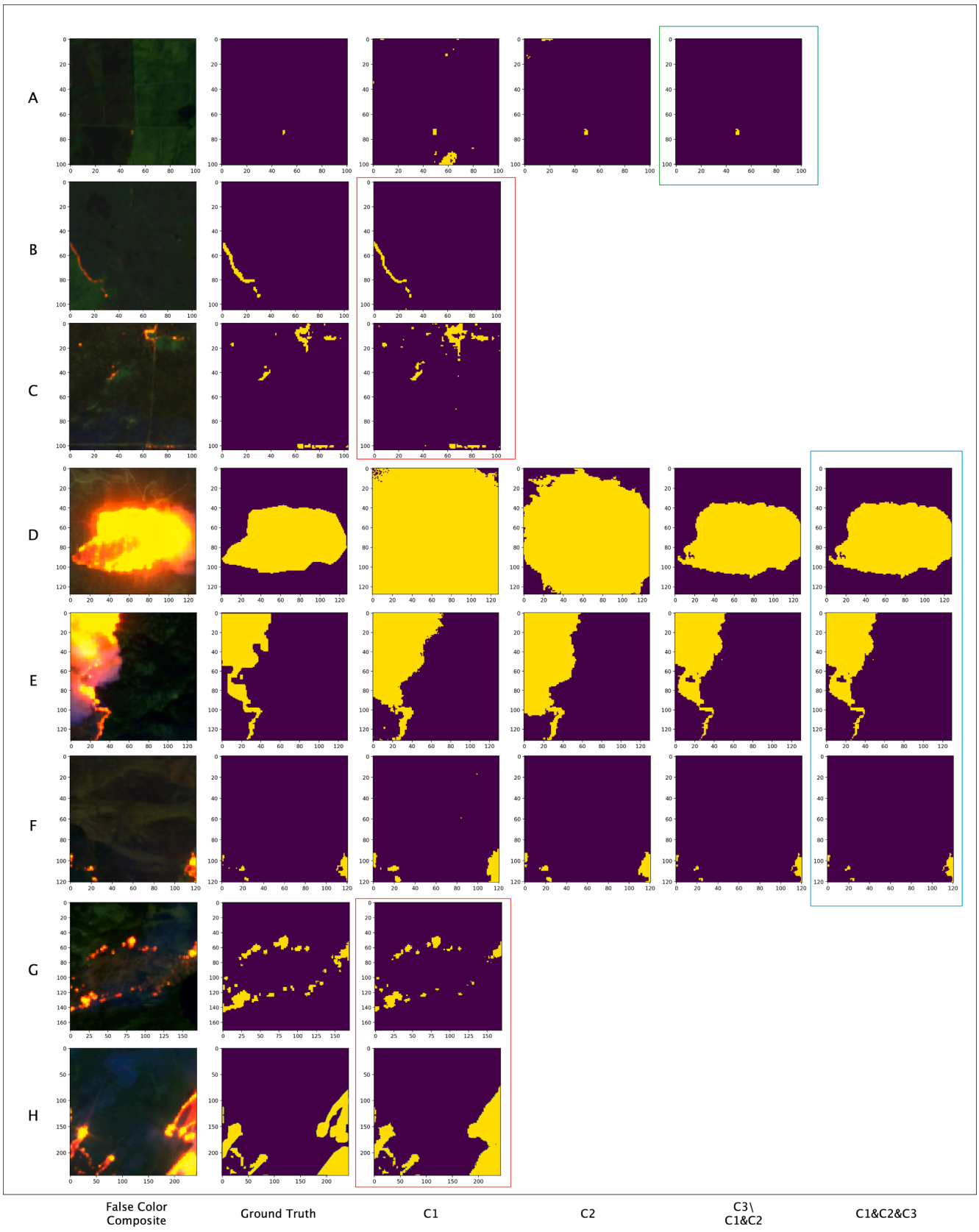

Fig. 7. The first two columns are patch images clipped from the original subset with 20 meters of spatial resolution (RGB: B12, B11, and B4) and the corresponding masks (ground truth, GT), respectively. The final column for each row is the final active fire map based on the AFD-S2 algorithm.

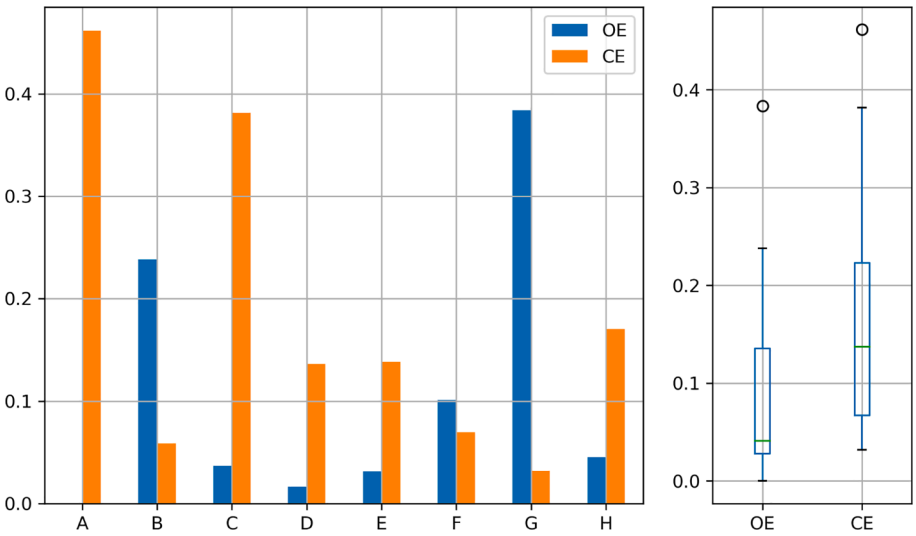

Fig. 8. OE and CE of active fire map produced based on AFD-S2 algorithms for each patch in the left subfigure. The other subfigure on the right-hand shows the dispersion of OE and CE considering all 8 patches. The green line denotes the median value. The 75th and 25th percentiles are represented by the corresponding top and bottom box edges, respectively. And the black circle indicate outliers.

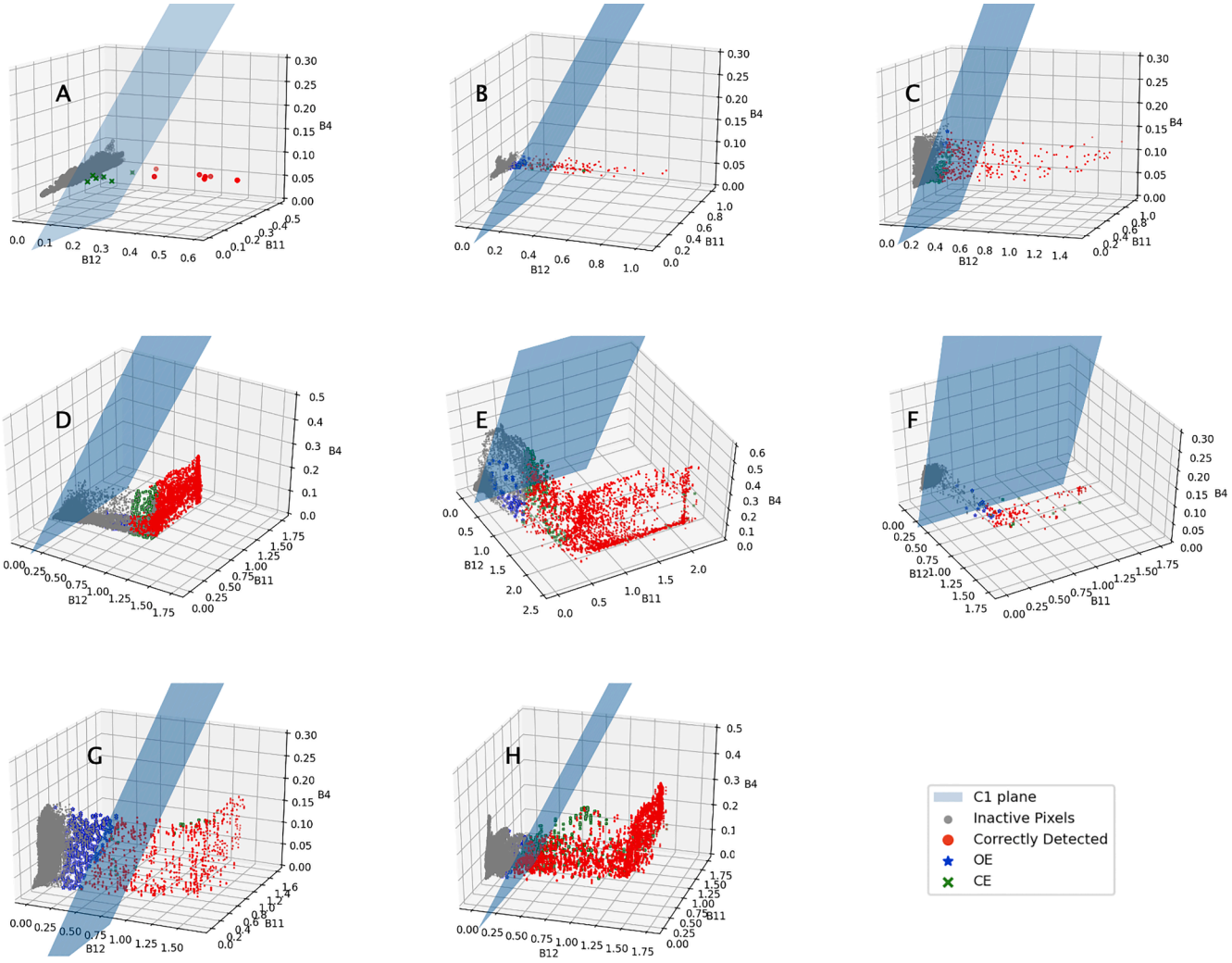

Fig. 9. 3D distribution over B4, B11 and B12 reflectance to highlight the OE and CE of active fire detection results in Fig. 7.

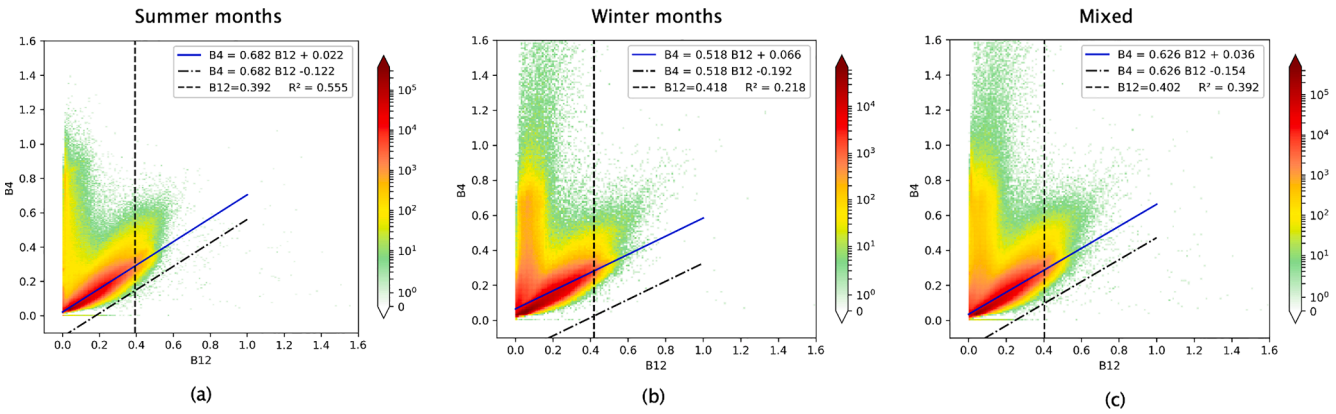

Fig. 10. Spectral scatterplots of 11,512,369 and 5,394,412 Sentinel-2 TOA reflectance values (B4 vs B12) extracted over ROIs from three winter and three summer months in (a) and (b), respectively. The mixed scatterplot in (c) is produced based on all samples together.

burning hotpots (mainly smoldering fires) within the burned scar that is hard to be. On the other hand, the high CE in patch A is due to a few actively burning pixels that are totally overlaid by the AFD-S2 algorithm. The limited visual GT that ignored some cool burning pixels results in the high CE in patch C. Conversely, more actively burning pixels that can be detected in patch C also prove the efficiency of AFD-S2 in cool smoldering fire detection in Tropical & Subtropical Grasslands, Savannas & Shrublands.

To avoid the effect of uncertainty of visual inspection, the algorithm accuracy was determined as the median values of CE and OE (0.14 and 0.04 respectively), as the green line indicated in the dispersion boxplot in Fig. 8, it would be found that medium CE stays under 0.15 with an outlier value from patch A. On the other hand, one outlier of patch G in OE's boxplot also does not affect the performance of the AFD-S2 algorithm.

The 3-dimensional (3D) distribution of B4, B11, and B12 are plotted in Fig. 9 to highlight OE and CE in the different patches. B12 saturates at different reflectance values in these subsets (1.0, 2.0, and 0.5 in D, E, and F, respectively). Regarding G and H, the saturated level of B12 is close to 1.4. From A to C, the tropical forest fires seem no saturated pixels for active fire due to the cool fires with low temperature.

There are only a few active fire points (7 pixels in GT) in patch A, therefore, 6 more pixels around the hotspots are misclassified as anomaly points in the final active fire map, leading to the pretty high CE of about 0.46. The high OE in patch B is mainly caused by the overestimation of visual inspection, it can be seen that some pixels tagged as OE in blue should have been omitted since they seem to be inactive pixels with a strong connection to gray pixels. Conversely, the CE in patch C is caused by the underestimation of GT since few pixels colored as CE in green should have been regarded as real active fire hotspots, accounting for their tight relationship with the correctly detected pixels in red. Patches from D to H have the same "L" structure in the distribution of B11 and B12 where the majority of identified active fire pixels saturate B12 in Mediterranean Forests, Woodlands & Scrub, Temperate Conifer Forests, and Boreal Forests/Taiga. Therefore, in these biomes with saturated B12, **C3** would dominate the importance among criteria. In detail, some CE pixels in patch D represent a low value of B11 but a high value B12, which implies the high temperature in the hot ashes area. Conversely, relatively high OE in G is caused by the tight constraint of Eq. (2) which underestimated some actively burning hotspots with low values of B12. Interestingly, the high CE in patch H is led by high temperature in the adjacent pixels around active fire spots, which is difficult to filter out.

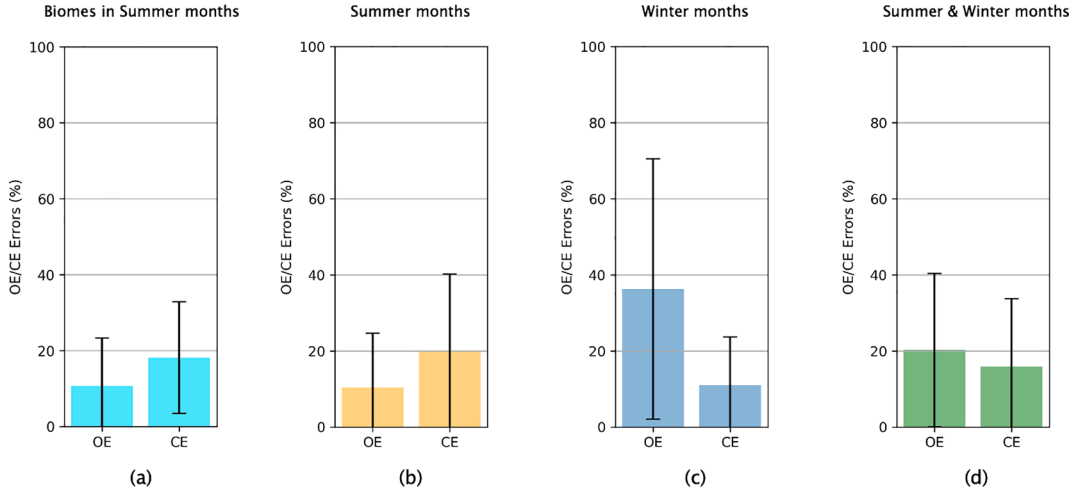

Fig. 11. The error bar of illustrative results in different data source based on the AFD-S2 algorithms. (a) the average values of OE and CE using biome-based AFD-S2 with summer months data (i.e. results in Fig. 8). The error bar lines with one standard deviation are in black. (b) the average values of OE and CE using uniform AFD-S2 boundaries of **C1**, as presented in Fig. 10(a), based on all samples in summer months. (b) the average values of OE and CE using uniform AFD-S2 boundaries of **C1**, as given in Fig. 10(b), based on all samples in winter months. (d) the average values of OE and CE using uniform AFD-S2 boundaries of **C1**, as shown in Fig. 10(c), based on all samples in summer and winter months.

4.4. The impacts of observation samples in different season

Apart from summer months, the observation samples in winter months were collected between 2018–11-01 and 2019–02-01 across the same 14 regions or countries. In the GOLI algorithm, the data acquired in winter months and summer months across the conterminous United States were mixed for the OLS regressions as the fixed threshold boundaries for global areas. To investigate the impacts of observation samples on AFD-S2 algorithm parameterizations, Fig. 10 showed the scatterplots based on all data in summer, winter, or both of them, respectively. It is observed that OLS with data in summer months has the highest R^2, conversely, data in winter months have the lowest one. The reason might be the low reflective values from ice or snow (particularly in Siberia and BC, Canada) in winter. It is expected that parameters of scatterplot (e.g. coefficient, intercept, and R^2 of OLS regression) with mixed data are between the parameters from summer and winter.

Applied these algorithm parameterizations in Fig. 10 to illustrative patches, the validation results can be summarised in Fig. 11. It can be concluded that the biome-based AFD-S2 algorithm with data in the summer months shows acceptable accuracy on average with a good trade-off between OE and CE. In detail, the biome-based parameterizations have similar accuracy with straightforward parameterizations using all data in summer months, but relatively lower average OE and CE with lower standard deviation (error bar lines in black). On the other hand, data in winter has much tight threshold boundaries than others, causing the highest OE due to underestimation on active fire hotspots, which conversely results in the lowest CE. Similarly, mixing summer and winter data can lower OE but still relatively high. Overall, to keep the trade-off between OE and CE, the data in summer months related to the fire season can optimize the AFD-S2 algorithm parameterizations rather than a mixture with data in winter months. To simplify the practical applications to some extent, the uniform AFD-S2 algorithm parameterizations only with summer data could also reach relatively high accuracy globally. And the biome-based AFD-S2 algorithm is recommended to apply in regional fire-prone areas with more reliable accuracy.

5. Discussion

This study explored the capability of Sentinel-2 to detect active fire and proposed a multi-criteria algorithm that takes into account the different biomes to reduce commission and omission errors. The Sentinel-2 sensor capabilities avoids the oversaturation artifacts that occur in Landsat-8 SWIR Band 6 and 7, which simplifies the implementation of active fire algorithms. The proposed AFD-S2 takes advantage of the higher spatial resolution of Sentinel-2 imagery than previous low-resolution sensors (e.g. MODIS). Multi-criteria thresholds were defined statistically based on 11,512,369 reflectance values extracted from Sentinel-2 tiles across 14 fire-prone regions during the summer period. The basic criterion was derived from 3σ prediction interval of OLS regression for each of the considered biomes. More criteria in the most challenging biomes were introduced to reduce the OE and CE.

Performance assessment is very challenging for active fire detection algorithms due to the lack of independent reference data. Optimally, active fire detection algorithms should achieve high accuracy with low CE and OE, but the CE is generally higher, and it's more challenging to reduce OE. In this study, AFD-S2 realized an acceptable trade-off between OE and CE, making it suitable for the majority of active fire monitoring applications. Multi-temporal tests used in Kumar and Roy (2018) and Schroeder et al. (2016) are skipped in this study because these processes are time-consuming to ingest all the multi-spectral tiles in the previous six months. It increases preprocessing time and constraints the future NRT applications especially for the next Earth observation satellite with an onboard data processor that will only have limited storage for previous scenes.

Like the Landsat sensors, the multi-spectral Sentinel-2 sensors are not specifically designed for active fire detection. It should be noted that Landsat-8 and Sentinel-2 data are better suited for burned area mapping than active fire/thermal anomaly detection due to low temporal coverage but high spatial resolution, thus they are mainly used as the complementary data source for existing coarse resolution polar-orbiting sensors. The Landsat-8 or Sentinel-2 reflectance-based active fire detection algorithms may still suffer from the potential CE. For example, due to hot and highly reflective building roofs that would occupy a large proportion of the pixel, commission errors occur at even VIIRS resolution (375 m) (Schroeder et al., 2014) and especially at Landsat-class resolution data with small IFOV (Kumar and Roy, 2018). In addition, sun-glint over water would cause commission errors due to its high reflectance (Giglio et al., 2016). However, the AFD-S2 algorithm is a sub-optimal choice when the middle-infrared and thermal infrared wavelengths are not available to detect fires (Giglio et al., 2003; Wooster et al., 2012). Therefore, it would become a potential way to detect active fire in NRT through the fusion of Sentinel-2 and Landsat-8, even future Landsat-9 satellites. Using the cross-sensor transformation functions, it would be achievable to apply the AFD-S2 algorithm to other Landsat satellites. More importantly, AFD-S2 makes it promising to realize the medium resolution monitoring, along with the coarser indication in the hotspots provided by MODIS-like polar-orbiting and geostationary systems (Li and Roy, 2017; Loveland and Dwyer, 2012; Kumar and Roy, 2018). On the other hand, the main limitations were related to the uncertainty of visual inspection to obtain ground truth. To eliminate such limitations, further improvements shall be investigated.

6. Conclusion

This paper presented an active fire detection algorithm to identify unambiguous active fire pixels using Sentinel-2 data. Representative biome characterizing vegetation fuel and climate attributes is used as an ancillary standard for multiple criteria in specific fire-prone regions. The proposed algorithm is designed to make use of existing biome properties for the dynamic thresholds based on huge sets of observation samples to avoid invalid data or abnormal observation values. The AFD-S2 algorithm proposed here was applied to eight illustrative subsets of Sentinel-2 images covering the most typical fire-prone regions worldwide. Validation experiments demonstrated that the AFD-S2 algorithm could accurately capture the small active fire spots with medium CE and OE over 8 Sentinel-2 images around 0.14 and 0.04, respectively. The algorithm can be deployed for global fire monitoring whenever Sentinel-2 data is available with the already existing biome types properties (e.g. GEE platform).

The main advantages of the proposed algorithm can be summarized into three aspects. One is the wider observations sampled in 14 regions/countries around the world to produce a more reliable constraint-boundary based on the 3σ lower prediction interval of OLS regression of grouped biome data. The thresholds for various fire-induced biomes are adjustable with additional criteria for specific environments and corresponding typical vegetation. The other one is that there are no multi-temporal tests involved besides several criteria applied to the Sentinel-2 image and the algorithm can be easily adapted to future onboard applications. In addition, more rapid deployment is also suggested for global NRT monitoring based on the uniform AFD-S2 algorithm with one threshold boundaries from data in summer months.

CRediT authorship contribution statement

Xikun Hu: Conceptualization, data curation, investigation, methodology, validation, visualization, writing - original draft. **Yifang Ban:** Conceptualization, methodology, funding acquisition, supervision, writing - review & editing. **Andrea Nascetti:** Methodology, supervision, writing - review & editing.

Declaration of Competing Interest

The authors declare that they have no known competing financial interests or personal relationships that could have appeared to influence the work reported in this paper.

Acknowledgement

Xikun Hu was funded by the China Scholarship Council. The research is part of the 'EO-AI4GlobalChange' project funded by KTH Digital Futures. We acknowledge the use of data from Sentinel-2 operated by the Copernicus Programme, and from LANCE FIRMS operated by the NASA GSFC Earth Science Data and Information System (ESDIS). We thank anonymous reviewers for their helpful comments and thoughtful suggestions.

Appendix A. Summary of active fire sensors

See Table A.5.

Table A.5
Sensors and typical channels used in active fire detection.

Sensors	Channel number	Central wavelength (μm)	Resolution (m)	Reference
MODIS	1	0.65	250	(Giglio et al., 2016)
	2	0.86	250	
	7	2.1	500	
	21	4.0	1000	
	22	4.0	1000	
	31	11.0	1000	
	32	12.0	1000	
VIIRS	I1	0.64	375	(Schroeder et al., 2014)
	I2	0.865	375	
	II3	1.61	375	
	I4	3.75	375	
	I5	11.45	375	
	M13	4.05	750	
FengYun-3C VIRR	3	3.74	1000	(Lin et al., 2018)
	4	10.80	1000	
	S2	0.66	500	
	S3	0.87	500	
Sentinel-3 SLSTR	S5	1.61	500	(Wooster et al., 2012)
	S6	2.25	500	
	F1	3.74	1000	
	F2	10.85	1000	
ASTER	3 N	0.82	15	(Giglio et al., 2008)
	8	2.33	30	
Landsat-8 OLI	B1	0.44	30	(Schroeder et al., 2016) (Murphy et al., 2016) (Kumar and Roy, 2018)
	B4	0.66	30	
	B5	0.87	30	
	B6	1.61	30	
	B7	2.20	30	

References

Bond, W.J., Woodward, F.I., Midgley, G.F., 2005. The global distribution of ecosystems in a world without fire. New Phytol. 165, 525–538. https://doi.org/10.1111/j.1469-8137.2004.01252.x.

Bowman, D.M., Williamson, G.J., Abatzoglou, J.T., Kolden, C.A., Cochrane, M.A., Smith, A.M., 2017. Human exposure and sensitivity to globally extreme wildfire events. Nature Ecol. Evol. 1, 0058.

Government of Canada, N.R., 2020. Indicator: Forest fires. URL: https://www.nrcan.gc.ca/our-natural-resources/forests-forestry/state-canadas-forests-report/how-does-disturbance-shape-canad/indicator-forest-fires/16392.

Csiszar, I.A., Schroeder, W., 2008. Short-term observations of the temporal development of active fires from consecutive same-day etm+ and aster imagery in the amazon: Implications for active fire product validation. IEEE J. Sel. Top. Appl. Earth Obser. Remote Sens. 1, 248–253.

Davies, D.K., Ilavajhala, S., Wong, M.M., Justice, C.O., 2009. Fire information for resource management system: Archiving and distributing MODIS active fire data. IEEE Trans. Geosci. Remote Sens. https://doi.org/10.1109/TGRS.2008.2002076.

Dinerstein, E., Olson, D., Joshi, A., Vynne, C., Burgess, N.D., Wikramanayake, E., Hahn, N., Palminteri, S., Hedao, P., Noss, R., Hansen, M., Locke, H., Ellis, E.C., Jones, B., Barber, C.V., Hayes, R., Kormos, C., Martin, V., Crist, E., Sechrest, W., Price, L., Baillie, J.E., Weeden, D., Suckling, K., Davis, C., Sizer, N., Moore, R., Thau, D., Birch, T., Potapov, P., Turubanova, S., Tyukavina, A., De Souza, N., Pintea, L., Brito, J.C., Llewellyn, O.A., Miller, A.G., Patzelt, A., Ghazanfar, S.A., Timberlake, J., Klöser, H., Shennan-Farpón, Y., Kindt, R., Lillesø, J.P.B., Van Breugel, P., Graudal, L., Voge, M., Al-Shammari, K.F., Saleem, M., 2017. An Ecoregion-Based Approach to Protecting Half the Terrestrial Realm. doi:10.1093/biosci/bix014.

Drusch, M., Del Bello, U., Carlier, S., Colin, O., Fernandez, V., Gascon, F., Hoersch, B., Isola, C., Laberinti, P., Martimort, P., Meygret, A., Spoto, F., Sy, O., Marchese, F., Bargellini, P., 2012. Sentinel-2: ESA's Optical High-Resolution Mission for GMES Operational Services. Remote Sens. Environ. 120, 25–36. https://doi.org/10.1016/j.rse.2011.11.026.

ESA, 2019. Siberian wildfires. URL: https://www.esa.int/ESA_Multimedia/Images/2019/07/Siberian_wildfires.

Fernández-Manso, A., Fernández-Manso, O., Quintano, C., 2016. Sentinel-2a red-edge spectral indices suitability for discriminating burn severity. Int. J. Appl. Earth Obser. Geoinformat. 50, 170–175.

Gascon, F., Bouzinac, C., Thépaut, O., Jung, M., Francesconi, B., Louis, J., Lonjou, V., Lafrance, B., Massera, S., Gaudel-Vacaresse, A., Languille, F., Alhammoud, B., Viallefont, F., Pflug, B., Bieniarz, J., Clerc, S., Pessiot, L., Trémas, T., Cadau, E., De Bonis, R., Isola, C., Martimort, P., Fernandez, V., 2017. Copernicus Sentinel-2A calibration and products validation status. Remote Sensing 9. https://doi.org/10.3390/rs9060584.

Giglio, L., Csiszar, I., Restás, Á., Morisette, J.T., Schroeder, W., Morton, D., Justice, C.O., 2008. Active fire detection and characterization with the advanced spaceborne thermal emission and reflection radiometer (ASTER). Remote Sens. Environ. 112, 3055–3063.

Giglio, L., Descloitres, J., Justice, C.O., Kaufman, Y.J., 2003. An enhanced contextual fire detection algorithm for MODIS. Remote Sensing Environ. 87, 273–282. URL: http://linkinghub.elsevier.com/retrieve/pii/S0034425703001846, doi:10.1016/S0034-4257(03)00184-6.

Giglio, L., Justice, C.O., 2003. Effect of wavelength selection on characterization of fire size and temperature. Int. J. Remote Sens. 24, 3515–3520. https://doi.org/10.1080/0143116031000117056.

Giglio, L., Schroeder, W., Justice, C.O., 2016. The collection 6 MODIS active fire detection algorithm and fire products. Remote Sens. Environ. 178, 31–41. https://doi.org/10.1016/j.rse.2016.02.054.

Hall, J., Zhang, R., Schroeder, W., Huang, C., Giglio, L., 2019. Validation of GOES-16 ABI and MSG SEVIRI active fire products. Int. J. Appl. Earth Obs. Geoinf. 83, 101928. https://doi.org/10.1016/j.jag.2019.101928.

Huang, H., Roy, D.P., Boschetti, L., Zhang, H.K., Yan, L., Kumar, S.S., Gomez-Dans, J., Li, J., Huang, H., Roy, D.P., Boschetti, L., Zhang, H.K., Yan, L., Kumar, S.S., Gomez-Dans, J., Li, J., 2016. Separability analysis of Sentinel-2A Multi-Spectral Instrument (MSI) data for burned area discrimination. Remote Sensing 8, 873. https://doi.org/10.3390/rs8100873. URL: http://www.mdpi.com/2072-4292/8/10/873.

Justice, C.O., Giglio, L., Roy, D., Boschetti, L., Csiszar, I., Davies, D., Korontzi, S., Schroeder, W., O'Neal, K., Morisette, J., 2011. MODIS-derived global fire products. Remote Sensing Digital Image Process. 11, 661–679. https://doi.org/10.1007/978-1-4419-6749-7_29. URL: http://link.springer.com/10.1007/978-1-4419-6749-7_29.

Kaufman, Y.J., Justice, C.O., Flynn, L.P., Kendall, J.D., Prins, E.M., Giglio, L., Ward, D.E., Menzel, W.P., Setzer, A.W., 1998. Potential global fire monitoring from EOS-MODIS. J. Geophys. Res. Atmosph. https://doi.org/10.1029/98JD01644.

Kumar, S.S., Roy, D.P., 2018. Global operational land imager Landsat-8 reflectance-based active fire detection algorithm. Int. J. Digital Earth 11, 154–178. URL: https://www.tandfonline.com/action/journalInformation?journalCode=tjde20, doi:10.1080/17538947.2017.1391341.

Li, J., Roy, D.P., 2017. A global analysis of Sentinel-2a, Sentinel-2b and Landsat-8 data revisit intervals and implications for terrestrial monitoring. Remote Sensing. https://doi.org/10.3390/rs9090902.

Lin, Z., Chen, F., Niu, Z., Li, B., Yu, B., Jia, H., Zhang, M., 2018. An active fire detection algorithm based on multi-temporal FengYun-3C VIRR data. Remote Sens. Environ. 211, 376–387. https://doi.org/10.1016/j.rse.2018.04.027.

Loveland, T.R., Dwyer, J.L., 2012. Landsat: Building a strong future. Remote Sens. Environ. 122, 22–29. https://doi.org/10.1016/j.rse.2011.09.022.

Matson, M., Holben, B., 1987. Satellite detection of tropical burning in brazil. Int. J. Remote Sens. 8, 509–516. https://doi.org/10.1080/01431168708948657.

Murphy, S.W., de Souza Filho, C.R., Wright, R., Sabatino, G., Correa Pabon, R., 2016. HOTMAP: Global hot target detection at moderate spatial resolution. Remote Sens. Environ. https://doi.org/10.1016/j.rse.2016.02.027.

Navarro, G., Caballero, I., Silva, G., Parra, P.C., Vázquez, Á., Caldeira, R., 2017. Evaluation of forest fire on Madeira Island using Sentinel-2A MSI imagery. Int. J. Appl. Earth Obser. Geoinformat. 58, 97–106. URL: http://linkinghub.elsevier.com/retrieve/pii/S0303243417300296, doi:10.1016/j.jag.2017.02.003.

Quintano, C., Fernández-Manso, A., Fernández-Manso, O., 2018. Combination of landsat and sentinel-2 msi data for initial assessing of burn severity. Int. J. Appl. Earth Obser. Geoinformat. 64, 221–225.

Roberts, G., Wooster, M.J., 2014. Development of a multi-temporal Kalman filter approach to geostationary active fire detection & fire radiative power (FRP) estimation. Remote Sens. Environ. 152, 392–412. https://doi.org/10.1016/j.rse.2014.06.020.

Roteta, E., Bastarrika, A., Padilla, M., Storm, T., Chuvieco, E., 2019. Development of a Sentinel-2 burned area algorithm: Generation of a small fire database for sub-Saharan Africa. Remote Sensing Environ. 222, 1–17. URL: https://www.sciencedirect.com/science/article/pii/S0034425718305649, doi:10.1016/J.RSE.2018.12.011.

Scholes, R.J., Kendall, J., Justice, C.O., 1996. The quantity of biomass burned in southern Africa. J. Geophys. Res. Atmosph. 101, 23667–23676. https://doi.org/10.1029/96jd01623.

Schroeder, W., Oliva, P., Giglio, L., Csiszar, I.A., 2014. The New VIIRS 375m active fire detection data product: Algorithm description and initial assessment. Remote Sens. Environ. 143, 85–96. https://doi.org/10.1016/j.rse.2013.12.008.

Schroeder, W., Oliva, P., Giglio, L., Quayle, B., Lorenz, E., Morelli, F., 2016. Active fire detection using landsat-8/oli data. Remote Sensing Environ. 185, 210–220.

Setzer, A.W., Pereira, M.C., 1991. Amazonia biomass burnings in 1987 and an estimate of their tropospheric emissions. Ambio 20, 19–22. https://doi.org/10.2307/4313765.

Stroppiana, D., Pinnock, S., Gregoire, J.M., 2000. The global fire product: Daily fire occurrence from April 1992 to december 1993 derived from NOAA AVHRR data. Int. J. Remote Sens. 21, 1279–1288. https://doi.org/10.1080/014311600210173.

USGS, 2019. Landsat 8 Data Users Handbook. Nasa URL: https://landsat.usgs.gov/documents/Landsat8DataUsersHandbook.pdf.

Van Der Werff, H., Van Der Meer, F., 2016. Sentinel-2a msi and landsat 8 oli provide data continuity for geological remote sensing. Remote Sensing 8, 883.

Wikipedia, 2019. 2019 siberia wildfires. URL: https://en.wikipedia.org/wiki/2019_Siberia_wildfires.

Wooster, M.J., Xu, W., Nightingale, T., 2012. Sentinel-3 SLSTR active fire detection and FRP product: Pre-launch algorithm development and performance evaluation using MODIS and ASTER datasets. Remote Sens. Environ. https://doi.org/10.1016/j.rse.2011.09.033.

Yeung, J., 2019. Fires destroy more than 4.2 million wild acres in bolivia. URL: https://edition.cnn.com/2019/09/06/americas/bolivia-fires-intl-hnk-trnd/.

Zhang, H.K., Roy, D.P., Yan, L., Li, Z., Huang, H., Vermote, E., Skakun, S., Roger, J.C., 2018. Characterization of Sentinel-2A and Landsat-8 top of atmosphere, surface, and nadir BRDF adjusted reflectance and NDVI differences. Remote Sens. Environ. 215, 482–494. https://doi.org/10.1016/j.rse.2018.04.031.